J Neurophysiol 135: 534–546, 2026.
First published January 28, 2026; doi:10.1152/jn.00455.2025

american physiological society

JNP JOURNAL OF NEUROPHYSIOLOGY

RESEARCH ARTICLE

Cellular and Molecular Properties of Neurons

LHX2 regulates biophysical properties of astrocytes in the postnatal mouse hippocampus

Sanjna Kumari,[1]* Archana Iyer,[2]* Shubha Tole,[2] and Rishikesh Narayanan[1]

[1]*Cellular Neurophysiology Laboratory, Molecular Biophysics Unit, Indian Institute of Science, Bengaluru, India and*
[2]*Department of Biological Sciences, Tata Institute of Fundamental Research, Mumbai, India*

Abstract

The transcription factor LHX2 plays a critical role in multiple aspects of neuronal and glial development. In this study, we investigated the long-term electrophysiological consequences of *Lhx2* loss in astrocytes in the CA1 region of mouse hippocampus using a genetic strategy that ensured *Lhx2* was not disrupted in neurons. These mutant astrocytes exhibited a hyperpolarizing shift in their resting membrane potential, accompanied by a significant increase in input resistance and a significant decrease in input capacitance, together indicating altered biophysical properties compared with astrocytes in control mice. However, we found no significant alterations in the intrinsic electrophysiological characteristics of hippocampal CA1 neurons in mice with *Lhx2* mutant astrocytes compared with controls. Collectively, we identify LHX2 as a regulator of intrinsic membrane properties of hippocampal astrocytes.

NEW & NOTEWORTHY Astrocytes play a vital role in regulating neural circuit homeostasis, yet the transcriptional mechanisms governing their electrophysiological properties remain underexplored. Here, we identify the LIM-homeodomain transcription factor LHX2 as a key regulator of intrinsic electrical properties of astrocytes in the hippocampus. We demonstrate that deletion of *Lhx2* from postnatal astrocytes and their progenitors alters astrocytic membrane biophysics in adulthood, but this did not have noncell-autonomous effects on the intrinsic properties of CA1 pyramidal neurons.

astrocytes; electrophysiology; intrinsic excitability; Lhx2; pyramidal neurons

INTRODUCTION

LHX2 is a pleiotropic transcription factor that has been implicated in multiple facets of cortical development (reviewed in Ref. 1). LHX2 expression is detected in both gliogenic progenitors and differentiated astrocytes throughout development and into adulthood (2). Loss of LHX2 in gliogenic progenitors at birth results in astrocytes that display upregulation of GFAP and transcriptomic signatures associated with reactive astrocytes, even in the absence of injury. These observations demonstrated that LHX2 plays an ongoing role in maintaining cortical astrocyte homeostasis beyond initial development (2). Here, we examined the long-term electrophysiological consequences of astrocyte-specific *Lhx2* loss on hippocampal astrocytes and neurons.

We administered tamoxifen to floxed *Lhx2* mice carrying the hGFAPCreERT2 driver at *postnatal day 1* (*P1*). By this time point, as neurogenesis is complete, Cre-mediated recombination and *Lhx2* deletion are limited to astrocytic progenitors and differentiated astrocytes, while neurons are spared. We examined the electrophysiological properties of adult CA1 astrocytes that originated from P1 progenitors lacking *Lhx2*. Our analysis revealed that *Lhx2*-mutant astrocytes exhibited a significant hyperpolarizing shift in their resting membrane potential compared with controls, indicating altered ionic homeostasis. Importantly, these mutant astrocytes showed a marked increase in input resistance accompanied by a significant reduction in input capacitance, suggesting changes in their excitability and other functional characteristics that could impact their physiological roles within neural circuits. These observations are in contrast to the absence of changes in the biophysical properties of cortical astrocytes (2).

To assess whether deletion of *Lhx2* in astrocytes also influenced neurons, we recorded intrinsic properties of CA1 pyramidal neurons from the same mice group. Our data

*S. Kumari and A. Iyer contributed equally to this work.
Correspondence: R. Narayanan (rishi@iisc.ac.in); S. Tole (shubhatole@gmail.com).
Submitted 11 September 2025 / Revised 25 September 2025 / Accepted 23 January 2026

showed no significant differences in the subthreshold and suprathreshold electrophysiological properties of these neurons, including resting membrane potential, input resistance, or action potential firing characteristics, when compared with neurons in control animals. These observations showed that the intrinsic electrical properties of hippocampal pyramidal neurons remained unaffected despite altered biophysical properties of astrocytes where *Lhx2* was deleted.

In summary, our results demonstrate that early astrocytic-specific loss of *Lhx2* alters the biophysical properties of adult hippocampal astrocytes, without significantly altering those of CA1 pyramidal neurons.

MATERIALS AND METHODS

The mouse line, experimental procedures, and reagents used in this study are identical to descriptions in Iyer et al. (2) and are detailed here.

Ethical Approval

All experiments reported in this study were reviewed and approved by the Institute Animal Ethics Committee of the Indian Institute of Science, Bangalore, and Institutional Animal Ethics Committee of the Tata Institute of Fundamental Research (TIFR-IAEC). Animals were provided ad libitum food and water and were housed with an automated 12:12-h light-dark cycle, with the facility temperature maintained at 23°C. Both committees ensured that all animal studies were conducted in accordance with ethical guidelines.

Mice

The *Lhx2*$^{lox/lox}$ mouse line used in this study has been previously described in Mangale et al. (3). hGFAPCreERT2 (Strain No. 012849), and *Ai9* reporter mouse line (Strain No. 007909) are purchased from the Jackson laboratory. The *Lhx2* floxed allele (3) was generated using a targeting construct designed to recapitulate the *Lhx2* null animal (4). This mutant was created by targeted disruption of exons 2 and 3 of *Lhx2* that encode the LIM domains and the domain linking the LIM domains and homeodomain of *Lhx2*. Splicing between exons one and four results in a frameshift such that no homeodomain-containing peptide can be produced (4). Only exon 1 is in-frame, which encodes neither the LIM domains nor the HD. In previous work, we showed that immunostaining for LHX2 in hGFAPCreERT2:: *Ai9*:: *Lhx2*$^{lox/lox}$ brains shows no detectable LHX2 protein in the *Ai9*/+ astrocytes [Supplemental Fig. S1, *A*–*C*, of Iyer et al. (2)]. Mice homozygous for floxed alleles of *Lhx2*$^{lox/lox}$ and Ai9 reporter (*Lhx2*$^{lox/lox}$; *Ai9*/Ai9) were crossed with mice carrying Cre recombinase driven by the human GFAP promoter hGFAPCreERT2/+; *Lhx2*$^{lox/lox}$) to generate *Lhx2* conditional knockout (cKO) (hGFAPCreERT2/+; *Lhx2*$^{lox/lox}$; *Ai9*/+). This line was previously validated to demonstrate that administration of tamoxifen at *P1* results in efficient recombination of the floxed *Lhx2* allele such that at *P3* and *P5*, no LHX2 protein is detectable in Ai9+ astrocytes in the cortex and in the hippocampus, and no transcript corresponding to Exons 2 and 3 are seen in FACS-sorted astrocytes by P3 [see Supplemental Fig. 1, *A*–*E*, of Iyer et al. (2)].

Controls were hGFAPCreERT2 animals crossed to *Ai9/Ai9* animals. Animals of either sex were used in the study. All animals were kept at an ambient temperature and humidity, with a 12-h light-dark cycle and food available ad libitum. Noon of the day of the vaginal plug was designated as *embryonic day 0.5* (*E0.5*). The age of mice used for these experiments was 6–7 mo.

Primers used for genotyping were:
Detection of Cre for hGFAPCreERT2
Cre F: 5′ATTTGCCTGCATTACCGGTC-3′,
Cre R: 5′ATCAACGTTTTCTTTTCGG-3′.
Cre-positive DNA shows a band at 350 bp.
Lhx2 lox/lox F: 5′ACCGGTGGAGGAAGACTTTT3′,
Lhx2 lox/lox R: 5′CAGCGGTTAAGTATTGGGACA3′.
The band sizes for this PCR are as follows: Wild-type: 144 bp, Lhx2 floxed allele: 188 bp.

Tamoxifen Administration

Tamoxifen (Sigma, T5648) was prepared in corn oil (Sigma, C82687) with a concentration of 20 mg/mL and dissolved overnight at 37°C on a shaker. Cre-positive pups and the dam were administered Tamoxifen at 40 mg/kg at *P1*.

Tissue preparation.

P14 wildtype animals were administered Thiosol (0.5 mg/mL) at 0.04 mg/kg as an intraperitoneal injection to be anesthetized and transcardially perfused with 4% (wt/vol) paraformaldehyde in phosphate buffer, followed by overnight fixation. Before sectioning, they were transferred to 30% (wt/vol) sucrose-PBS for cryoprotection during the sectioning process. The brains were sectioned at 40 µm using a freezing microtome (Leica SM2000R).

Immunofluorescence.

Brains were sectioned and processed in a four-well plate for immunofluorescence. Antigen retrieval was performed at 90–95°C in 10 mM sodium citrate buffer (pH 6.0) for 10 min. Following this step, sections were subjected to a blocking solution comprising 5% (vol/vol) horse serum in phosphate buffer with 0.3% (vol/vol) Triton X-100 (0.1% for P5) (Sigma; X100) for 1 h at room temperature. Incubation with primary antibody was performed in a phosphate buffer containing 0.3% or 0.1% (vol/vol) Triton X-100 and 2.5% (vol/vol) horse serum at 4°C overnight. The following day, sections were washed in phosphate buffer thrice for 5 min each, followed by the appropriate secondary antibody (prepared in phosphate buffer containing 0.3% or 0.1% (vol/vol) Triton X-100) for 2 h at room temperature. This was followed by three washes for 5 min each in phosphate buffer and DAPI (Molecular Probes, Cat. No. D1306) staining for 10 min, after which the sections were washed with phosphate buffer thrice (5 min each). The slides were then mounted with Fluoroshield (Sigma, Cat. No. F6057 or F6182). The following antibodies were used (dilution 1:200):

Rabbit Lhx2 Merck Abe1402 lot number 3030529
Rabbit GFAP Sigma G9269 lot number O25M4843V

Image Acquisition and Analysis

Images were acquired with a FV1200 Olympus inverted confocal microscope equipped with an oil immersion objective

lens (×40). Confocal images were processed with the Fiji package of ImageJ (NIH).

Slice Preparation for In Vitro Patch-Clamp Recording

Electrophysiological experimental procedures were similar to previously established protocols (2, 5–7) and are detailed below. Five (3 males and 2 females) mice belonging to the control group between 4 and 7 mo old and four (2 males and 2 females) *Lhx2*$^{lox/lox}$ mice between 3 and 7 mo old were used for in vitro patch-clamp electrophysiology experiments.

Mice were anesthetized by intraperitoneal injection of a ketamine-xylazine mixture. After the onset of deep anesthesia, assessed by cessation of toe-pinch reflex, transcardial perfusion of ice-cold cutting solution was performed. The cutting solution contained (in mM) 2.5 KCl, 1.25 NaH_2PO_4, 25 $NaHCO_3$, 0.5 $CaCl_2$, 7 $MgCl_2$, 7 dextrose, 3 sodium pyruvate, and 200 sucrose (pH 7.3, ∼300 mosmol/kgH_2O) saturated with carbogen (95% O_2, 5% CO_2). Thereafter, the brain was removed quickly and 350-μm thick near-horizontal slices were prepared with a vibrating blade microtome (Leica Vibratome) while submerged in ice-cold cutting solution saturated with carbogen. The slices were then incubated for 10–15 min at 34°C in a holding chamber containing a holding solution (pH 7.3, ∼300 mosmol/kgH_2O) with the composition of (in mM) 125 NaCl, 2.5 KCl, 1.25 NaH_2PO_4, 25 $NaHCO_3$, 2 $CaCl_2$, 2 $MgCl_2$, 10 dextrose, and 3 sodium pyruvate saturated with carbogen. Thereafter, the slices were kept in the holding chamber at room temperature for at least 30 min before recordings started.

Whole Cell Current-Clamp Recordings

For electrophysiological recordings, slices were transferred to the recording chamber and were continuously perfused with carbogenated artificial cerebrospinal fluid (ACSF-extracellular recording solution) at a flow rate of 2–3 mL/min. All astrocytic and neuronal recordings were performed under current-clamp configuration at physiological temperatures (32–35°C) achieved through an inline heater that was part of a closed-loop temperature control system (Harvard Apparatus). The ACSF contained (in mM) 125 NaCl, 3 KCl, 1.25 NaH_2PO_4, 25 $NaHCO_3$, 2 $CaCl_2$, 1 $MgCl_2$, and 10 dextrose (pH 7.3; ∼300 mosmol/kgH_2O). Slices were first visualized under a ×10 objective lens to visually locate to the stratum pyramidale of hippocampal CA1 region. A ×63 water-immersion objective lens was used to perform patch-clamp recordings from CA1 pyramidal neurons and tdTomato-labelled astrocytes in CA1 region, through a Dodt contrast microscope (Carl Zeiss Axioexaminer). Whole cell current-clamp recordings were performed from neurons and astrocytes with a Dagan BVC-700A amplifier.

Borosilicate glass electrodes with electrode tip resistance between 4 and 8 MΩ were pulled (P-97 Flaming/Brown micropipette puller; Sutter) from thick glass capillaries (1.5-mm outer diameter and 0.86-mm inner diameter; Sutter) and used for patch-clamp recordings. The pipette solution contained (in mM) 120 K-gluconate, 20 KCl, 10 HEPES, 4 NaCl, 4 Mg-ATP, 0.3 Na-GTP, and 7 K_2-phosphocreatine (pH 7.3 adjusted with KOH; osmolarity ∼300 mosmol/kgH_2O). Series resistance was monitored and compensated online with the bridge-balance circuit of the amplifier. Experiments were discarded if the initial resting membrane potential was more depolarized than −50 mV or if series resistance rose above 50 MΩ, or if there were fluctuations in temperature and ACSF flow rate during the experiment. Voltages have not been corrected for the liquid junction potential, which was experimentally measured to be ∼8 mV. Voltage response of cells to a 250-pA hyperpolarizing current pulse was continuously monitored to observe and correct series resistance changes using the bridge balance circuit throughout the course of the experiment.

Pharmacological Blockers

All recordings were performed in presence of synaptic receptor blockers in the ACSF. Drugs and their concentrations used in the experiments were 10 μM 6-cyano-7-nitroquinoxaline-2,3-dione (CNQX), an AMPA receptor blocker, 10 μM (+) bicuculline and 10 μM picrotoxin, both $GABA_A$ receptor blockers, and 2 μM CGP55845, a $GABA_B$ receptor blocker (all synaptic blockers from Abcam) in the ACSF.

Electrophysiological Measurements

We characterized CA1 pyramidal neurons and astrocytes with several electrophysiological measurements using standard protocols (5–9), detailed below. Resting membrane potential, V_{RMP} was measured as the voltage at which the cell rested when no current was injected (Figs. 2, *A* and *B*, and 4, *A* and *B*). Input resistance (R_{in}) was measured as the slope of a linear fit to the steady-state voltage-current (*V*–*I*) plot obtained by injecting current pulses of amplitudes spanning −250 to 250 pA for astrocytes in steps of 50 pA (Fig. 2*A*) and −50 to 0 pA for neurons (Fig. 4*A*). We estimated membrane time constant τ_m of the mutant and control astrocytes by fitting double exponentials of the form $v = A_1\exp(-t/\tau_1) + A_2\exp(-t/\tau_2)$ to the astrocytic responses to the hyperpolarizing or depolarizing pulse current injection of 250 pA amplitude (10). The slowest of the two time constants obtained from the double exponential fit was assigned as the estimate of the membrane time constant, τ_m (10). We used the input resistance estimate (obtained from the same trace that was used to fit the double exponential) to compute estimates of input capacitance as $C_{in} = \tau_m/R_{in}$ (9) (Fig. 2, *C* and *D*).

Sag ratio was measured from the voltage response of the cell to a hyperpolarizing current pulse of 250 pA (Figs. 2*E* and 4*C*). Sag ratio was defined as $100 \times (1 - V_{SS}/V_{initial})$, where V_{SS} and $V_{initial}$ depict the steady-state and peak (during the initial 50-ms period after current injection) voltage deflections (from V_{RMP}), respectively. To assess temporal summation, five alpha excitatory postsynaptic potentials (α-EPSPs) with 50-ms interval were injected as currents of the form $I_\alpha = I_{max}\, t\, \exp(-\alpha t)$, with $\alpha = 0.1\ ms^{-1}$. Temporal summation ratio (S_α) in this train of five EPSPs (Figs. 2*F* and 4*D*) was computed as E_{last}/E_{first}, where E_{last} and E_{first} were the amplitudes of the last and first EPSPs in the train, respectively.

The chirp stimulus, a sinusoidal current with its frequency linearly spanning 0–15 Hz in 15 s and of constant amplitude, was used for characterizing the impedance profiles (Figs. 3*A*

and 4*E*). The voltage response of the cells to the chirp current stimulus injection was recorded at V_{RMP}. The ratio of the Fourier transform of the voltage response to the Fourier transform of the chirp stimulus formed the impedance profile. The frequency at which the impedance amplitude (Figs. 3*B* and 4*F*) reached its maximum was the resonance frequency (f_R). Resonance strength (Q) was measured as the ratio of the maximum impedance amplitude to the impedance amplitude at 0.5 Hz. Total inductive phase (Φ_L) was defined as the area under the inductive part of the impedance phase profile as a function of frequency (Figs. 3*C* and 4*G*).

No action potential firing was observed when higher currents, in the range of 250–1,250 pA in steps of 250 pA, were injected into the CA1 astrocytes. Pyramidal neurons of CA1 did elicit action potentials in response to rheobase current and above. Action potential (AP) firing frequency was computed by extrapolating the number of spikes obtained during a 700-ms current injection to 1 s. The amplitude of these pulse current injections was varied from 0 pA to 250 pA in steps of 50 pA to construct the firing frequency versus injected current (*f–I*) plot (Fig. 5*B*). In addition, to assess firing at higher current injections, we constructed *f–I* plots with high current injections ranging from 500 to 1,250 pA in steps of 250 pA (Fig. 5*B*).

Various AP-related measurements (5, 9, 11) were derived from the first action potential in the voltage response of the cell, resting at V_{RMP}, to a 250-pA pulse current injection (Fig. 5*C*). AP amplitude (V_{AP}) was computed as the difference between the peak voltage of the spike (V_{peak}) and V_{RMP} (Fig. 5*C*). The temporal distance between the timing of the first spike and the time of the current injection was defined as latency to the first spike T_{1AP}. The duration between the first and the second spikes was defined as the first interspike interval T_{1ISI}. AP half-width (T_{APHW}) was the temporal width measured at the half-maximal points of the AP peak concerning V_{RMP}. The maximum and minimum rate of change of voltage (dV/dt) of the AP temporal derivatives was calculated from the temporal first derivative of the voltage trace. The voltage in the AP trace corresponding to the time point at which the dV/dt crossed 20 V/s was defined as the AP threshold V_{th} (Fig. 5, *D* and *E*).

Analyses of Electrophysiological Data and Statistics

All electrophysiological data acquisition and analyses were performed with custom-written software in IGOR Pro (WaveMetrics), and statistical analyses were performed using Wilcoxon rank-sum test in R computing package (http://www.r-project.org/).

RESULTS

Lhx2 is Expressed in Hippocampal Astrocytes

In mice, astrocyte production is initiated toward the end of neurogenesis, from *embryonic day* (E) *15.5* and peaks postnatally (12). LHX2 is detected in SOX2+ progenitors in the ventricular zone (VZ) and ALDH1L1+ hippocampal astrocytes (2). In the hippocampus, GFAP+ astrocytes were colabeled for LHX2 (Fig. 1). To examine the role of LHX2 in astrocytes, we used a floxed *Lhx2* mouse line (3) together with an hGFAPCreERT2 driver (13) and an Ai9 reporter (14).

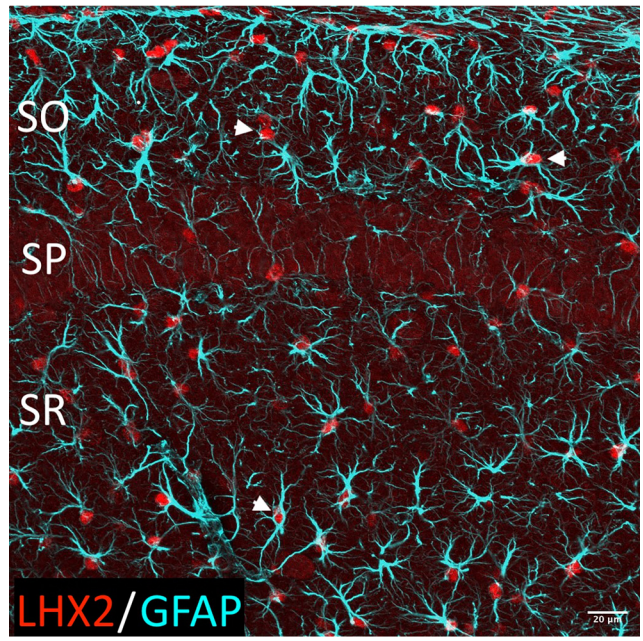

Figure 1. LHX2 is expressed in astrocytes in postnatal mouse hippocampus. At *P14*, hippocampal astrocytes are GFAP+LHX2+ (white arrowheads). $N = 3$ independent biological replicates. SO, *Stratum Oriens*; SP, *Stratum Pyramidale*; SR, *Stratum Radiatum*. Scale bar: 20 µm.

Control animals carried hGFAPCreERT2 with the Ai9 reporter. The hGFAP promoter drives expression in GFAP+ cells, which include progenitors and differentiated astrocytes. Tamoxifen was administered on *postnatal day 1* (*P1*). At this stage, neurogenesis is complete, therefore, neurons do not experience loss of *Lhx2,* but Cre-mediated recombination of *Lhx2* is driven in both astrogliogenic progenitors and differentiated astrocytes. The Ai9 reporter permits identification and scoring of *Lhx2*-mutant astrocytes. In earlier work using this model, we validated that the *Lhx2* transcript is lost in FACS-sorted astrocytes and LHX2 protein is absent in sections by P5 [see Supplemental Fig. S1 of Iyer et al. (2)].

Hyperpolarized Membrane Potential and Enhanced Gain in Adult CA1 Astrocytes upon Loss of *Lhx2*

We investigated the electrophysiological properties of astrocytes identified by Ai9 fluorescence in the control and $Lhx2^{lox/lox}$ mice using whole cell current-clamp recordings (Figs. 2 and 3). The labeled astrocytes did not elicit action potentials even for large depolarizing current injections up to 1,250 pA, thereby electrophysiologically confirming that these cells are not neurons. We observed significantly hyperpolarized resting membrane potentials for the mutant astrocytes as compared with the controls (Fig. 2, *A* and *B*). Input resistance of mutant astrocytes was found to be significantly higher than the controls, indicating enhanced electrical gain in hippocampal astrocytes with *Lhx2* deletion (Fig. 2, *A* and *B*, and Table 1). Although membrane time constants of control and mutant astrocytes were comparable (Fig. 2, *C* and *D*), input capacitance of mutant astrocytes was significantly lower than their control astrocytes (Fig. 2, *C* and *D*).

As there are lines of evidence for expression of resonating channels, such as HCN or *M*-type K^+ channels, in

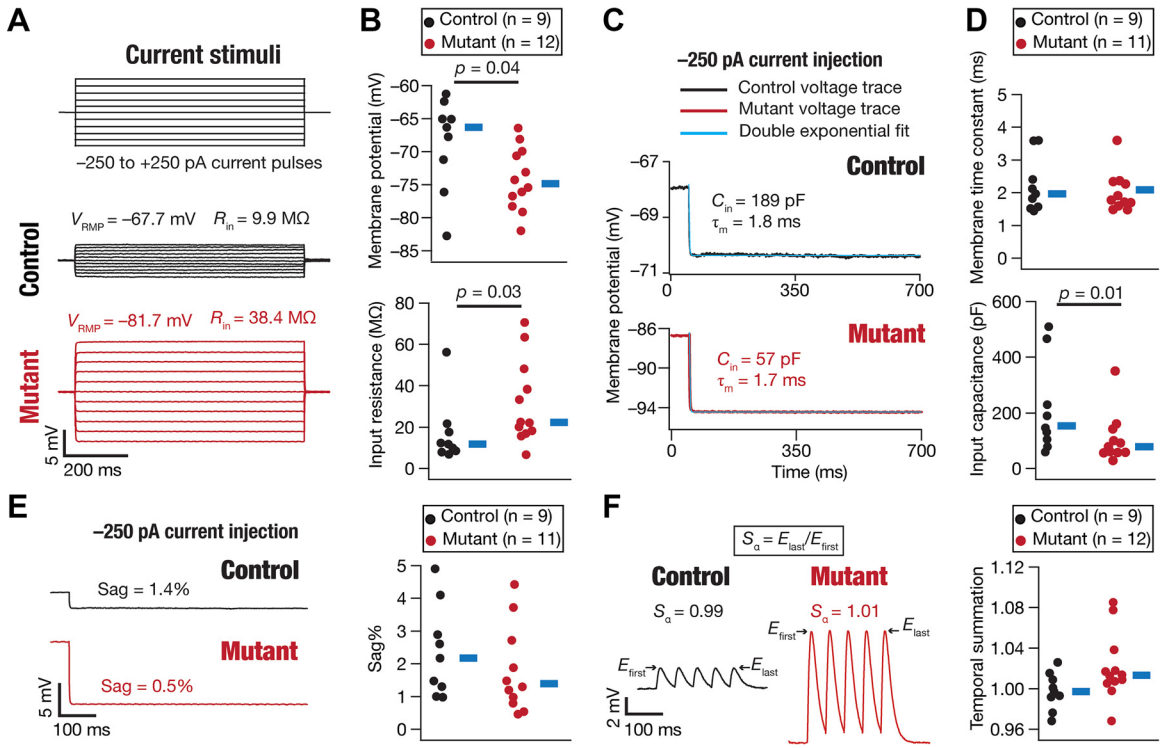

Figure 2. Adult hippocampal *Lhx2*-mutant astrocytes exhibited hyperpolarized resting potential and showed higher steady-state gain and reduced input capacitance compared to control mice. *A*: example voltage responses of control and mutant astrocytes to pulse current injections ranging from −250 pA to + 250 pA in steps of 50 pA (*top*), used for computing input resistance (R_{in}) (*bottom*). *B*: beeswarm plots of resting membrane potential (V_{RMP}, *top*) and input resistance (R_{in}, *bottom)* obtained from control and mutant astrocytes. *C*: plot illustrating a double exponential fit (blue) applied to voltage responses to a 250-pA hyperpolarizing current pulse from the example control (black) and mutant (red) astrocytes. The fit parameters for the example control astrocyte were input resistance R_{in} = 9.6 MΩ, membrane time constant τ_m = 1.8 ms, and local input capacitance C_{in} = 189 pF (*top*). The fit parameters for the example mutant astrocyte were input resistance R_{in}= 30.8 MΩ, membrane time constant τ_m = 1.7 ms, and local input capacitance C_{in} = 57 pF (*bottom*). *D*: beeswarm plot of membrane time constant (ms) (P = 0.71) and input capacitance (pF) (P = 0.01) calculated from all control and mutant astrocytes. *E*, *left*: traces showing voltage responses to a 250-pA hyperpolarizing pulse current of the example control and mutant astrocytes. Sag ratio was computed as the ratio between the initial peak and the steady-state voltage deflection. *Right*: beeswarm plot of sag ratio (P = 0.2) computed from all control and mutant astrocytes. *F*, *left*: train of five excitatory postsynaptic potentials (α-EPSPs) recorded from example control and mutant astrocytes. Temporal summation (S_α) was calculated as the ratio between the last and the first EPSP amplitudes. *Right*: beeswarm plot of S_α (P = 0.058) recorded from all control and mutant astrocytes. All illustrative example traces in this figure were taken from a single control and a single mutant astrocyte. The thick blue lines in all beeswarm plots represent the respective median values. *n* (9 for controls and 11/12 for mutants) represents the number of total astrocytes recorded from the CA1 region. All *P* values correspond to the outcomes of the Wilcoxon rank-sum test. Table 1 summarizes the means ± SE, and *P* values for measurements reported in this figure.

astrocytes (15, 16), we asked if this change in input resistance could be because of changes in such ion channels. To do this, we first asked if sag and temporal summation, two measures reflective of changes in resonating conductances (17–22), were different in control versus mutant astrocytes. We found that these measurements were not significantly different between control and mutant astrocytes (Fig. 2, *E* and *F*, and Table 1).

Although pulse current inputs are widely used to characterize steady-state cellular gain, they do not provide insights about how cells respond to time-varying inputs that are observed under in vivo conditions. In addition, hippocampal astrocytes could receive oscillatory current inputs in different frequency bands that are prevalent in the hippocampus (23–25) through ionotropic receptors that they express (26, 27). Although frequency-dependent excitability measures are widely used in analyzing neuronal properties (8, 9, 19, 28, 29), astrocytes have surprisingly not been characterized with time-varying current signals. We characterized frequency-dependent response properties of astrocytes with the chirp current stimulus with linearly increasing frequency from 0 to 15 Hz (5–9). In striking contrast with hippocampal pyramidal neurons that show strong frequency-dependent gain in this range of frequencies (8, 9, 19, 28), we found the gain of astrocytes to vary only by a few MΩ through the 0–15-Hz range (Fig. 3*B*). In addition, the impedance profile did not show strong resonance in astrocytes. Importantly, impedance phase was close to zero for the measured set of frequencies, implying a lack of strong capacitive filtering of the current inputs (Fig. 3*C*). We note this to be consistent with the small values of charging time constant in astrocytic responses to pulse current injections (Fig. 2, *C* and *D*).

To compare frequency-dependent response properties of control and mutant astrocytes, we computed several measurements from the impedance amplitude and phase profiles of these astrocytes. We found that maximal impedance amplitude $|Z|_{max}$, resonance frequency f_R, resonance strength Q from the impedance amplitude profile were not significantly different between control and mutant astrocytes (Fig. 3*D* and Table 1). We found a significant reduction in total inductive phase Φ_L computed from the impedance phase profile of mutant astrocytes (Fig. 3*D* and Table 1).

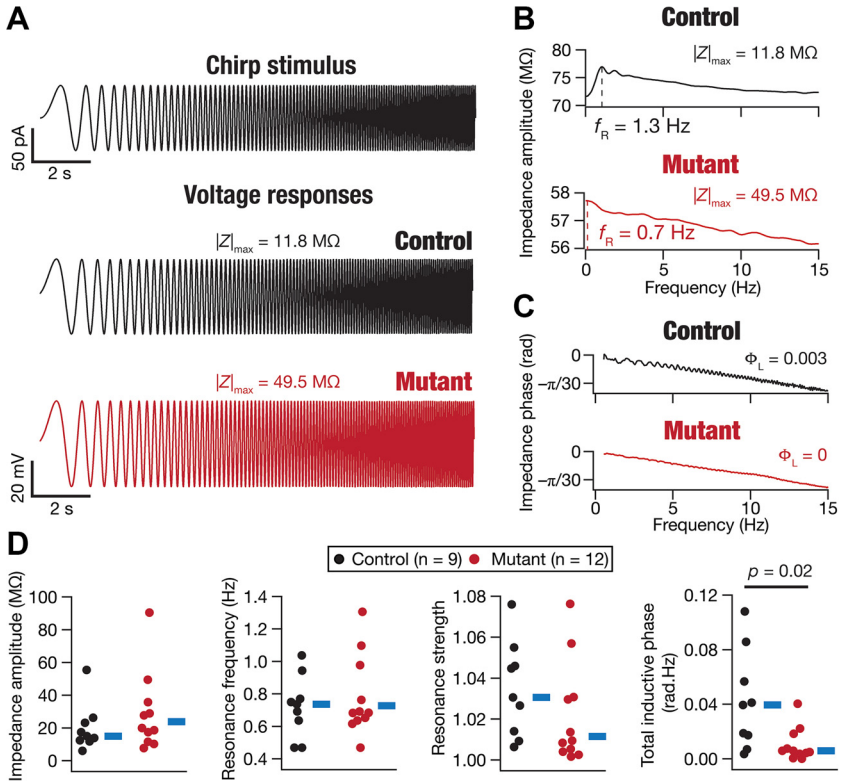

Figure 3. Impedance measurements from adult hippocampal astrocytes from control and *Lhx2*$^{lox/lox}$ mice. *A*, *top*: chirp current stimulus used for characterizing frequency-dependent characteristics of CA1 astrocytes. *Bottom*: voltage responses of the example control and mutant astrocytes to the chirp current stimulus. *B*: plots showing impedance amplitude profiles of control and mutant astrocytes with resonance frequency (f_R) and maximum impedance amplitude ($|Z|_{max}$) depicted. *C*: plots showing impedance phase profiles of control and mutant astrocytes with total inductive phase (Φ_L) depicted. *D*: beeswarm plots of maximum impedance amplitude $|Z|_{max}$, resonance frequency f_R, resonance strength Q, and total inductive phase Φ_L calculated for all control and mutant astrocytes. $P = 0.37$ for $|Z|_{max}$, $P = 1$ for f_R, $P = 0.17$ for Q, and $P = 0.02$ for Φ_L. All illustrative example traces in this figure were taken from a single control and a single mutant astrocyte. The thick blue lines in all beeswarm plots represent the respective median values. *n* (9 for controls and 12 for mutants) represents the number of total astrocytes recorded from the CA1 region. All *P* values correspond to the outcomes of the Wilcoxon rank-sum test. Table 1 summarizes the means ± SE, and *P* values for measurements reported in this figure.

Together, these observations demonstrate significant changes in resting membrane potential and steady-state gain of *Lhx2* mutant CA1 astrocytes as compared with the controls.

Intrinsic Properties of Adult CA1 Pyramidal Neurons Were Invariant to P1 Lhx2 Deletion

Furthermore, we sought to investigate if deletion of *Lhx2* in astrocytes had any effect on the electrophysiological properties of CA1 pyramidal neurons. We recorded basic electrophysiological properties of CA1 pyramidal neurons from the control and *Lhx2*$^{lox/lox}$ mice. We found resting membrane potential (Fig. 4, *A* and *B*), input resistance (Fig. 4, *A* and *B*), sag (Fig. 4*C*), and temporal summation ratio (Fig. 4*D*) comparable and not significantly different between the control and *Lhx2*$^{lox/lox}$ groups (Table 2). We characterized the resonance properties of pyramidal neurons using chirp stimulus whose frequency linearly increases from 0 to 15 Hz (Fig. 4, *E* and *F*). We found CA1 pyramidal neurons from both control and *Lhx2*$^{lox/lox}$ mice to manifest membrane potential resonance around 2–8 Hz, a range that is well established in rodent CA1 pyramidal neurons (8, 9, 28, 30, 31). Maximal impedance amplitude $|Z|_{max}$, resonance frequency f_R, and resonance strength Q, and total impedance phase Φ_L (Fig. 4*G*) of neurons from control and *Lhx2*$^{lox/lox}$ mice were comparable (Fig. 4*H* and Table 2).

We next looked at the suprathreshold properties of the CA1 pyramidal neurons in control and *Lhx2*$^{lox/lox}$ mice. We did not see a significant change in the firing rates of these cells between the two groups for both lower and higher current injection protocols (Fig. 5, *A* and *B* and Table 2). However, the action potential amplitude was significantly reduced in the neurons from *Lhx2*$^{lox/lox}$ mice as compared with the controls (Fig. 5, *C* and *D* and Table 2). All other action potential measurements (peak, threshold, half-width, latency to first spike, interspike interval, maximum and

Table 1. *Statistical analyses of biophysical measurements of CA1 astrocytes from control and Lhx2*$^{lox/lox}$ *mice*

	Measurements	Control	Mutant	*P* Value
1	Resting membrane potential, V_{RMP} (mV)	−68.6 ± 2.3	−74.2 ± 1.4	**0.04**
2	Input resistance, R_{in} (MΩ)	17.0 ± 5.2	31.4 ± 5.8	**0.03**
3	Membrane time constant, τ_m (ms)	2.23 ± 0.3	2.0 ± 0.2	0.71
4	Input capacitance, C_{in} (pF)	213.7 ± 54.8	108 ± 27	**0.01**
5	Summation ratio of αEPSPs, S_α	1.00 ± 0.01	1.02 ± 0.01	0.05
6	Sag, %	2.4 ± 0.5	1.8 ± 0.4	0.22
7	Maximal impedance amplitude, $\|Z\|_{max}$ (MΩ)	20.2 ± 4.9	28.9 ± 7.2	0.37
8	Resonance frequency, f_R (Hz)	0.72 ± 0.06	0.78 ± 0.07	1
9	Resonance strength, Q	1.03 ± 0.01	1.02 ± 0.01	0.17
10	Total inductive phase (Φ_L)	0.04 ± 0.01	0.01 ± 0	**0.02**

Provided are the means ± SE values for the control and mutant group measurements. The *P* values correspond to the Wilcoxon rank-sum test. All *P* values less than 0.05 are highlighted in boldface font.

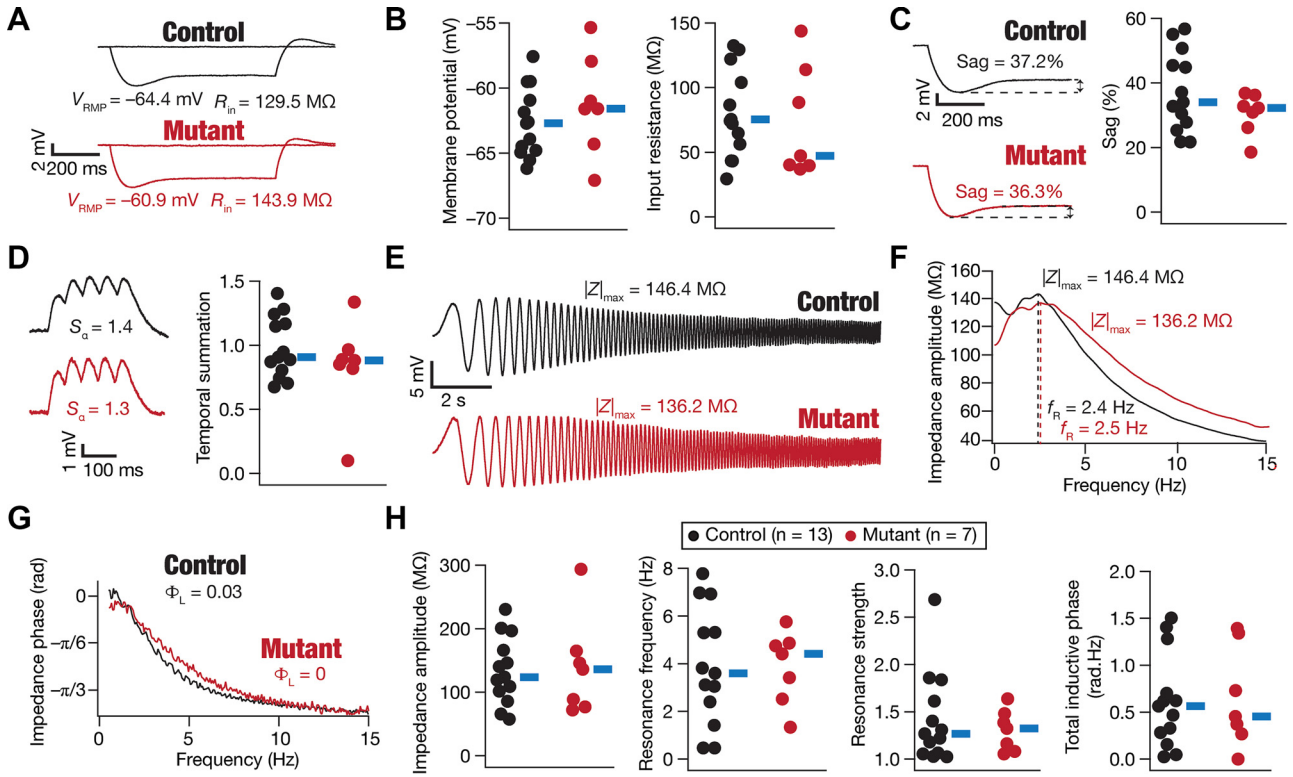

Figure 4. Subthreshold electrophysiological properties of adult CA1 pyramidal neurons showed no significant differences between control and *Lhx2*$^{lox/lox}$ mice. *A*: example voltage response of CA1 pyramidal neuron to pulse current injections of –50 pA and 0 pA used for computing input resistance (R_{in}). *B*: beeswarm plots of resting membrane potential (V_{RMP}, *left*, $P = 0.39$) and input resistance (R_{in}, *right*, $P = 0.58$) recorded from control and mutant CA1 pyramidal neurons. *C*, *left*: traces showing voltage response to a 250-pA hyperpolarizing pulse current for the example control (*top*) and mutant (*bottom*) neurons. Sag ratio was computed as the ratio between the initial peak and the steady-state voltage deflection. *Right*: beeswarm plot of sag ratio ($P = 0.35$) recorded from all control and mutant neurons. *D*, *left*: train of five excitatory postsynaptic potentials (α-EPSPs) recorded from example control (*top*) and mutant (*bottom*) neurons. Temporal summation (S_α) was calculated as the ratio between the last and the first EPSP amplitudes. *Right*: beeswarm plot of S_α ($P = 0.64$) recorded from all control and mutant neurons. *E*: voltage responses of the example control and mutant neurons to the chirp current stimulus. *F*: plots showing impedance amplitude profiles of control and mutant neuron with resonance frequency (f_R) and maximum impedance amplitude ($|Z|_{max}$) depicted. *G*: plots showing impedance phase profiles of control and mutant astrocytes with total inductive phase (Φ_L) depicted. *H*: beeswarm plots of maximum impedance amplitude $|Z|_{max}$, resonance frequency f_R, resonance strength Q, and total inductive phase Φ_L for all control and mutant CA1 pyramidal neurons. $P = 0.9$ for $|Z|_{max}$, $P = 1$ for f_R, $P = 1$ for Q, and $P = 1$ for Φ_L. All illustrative example traces in this figure were taken from a single control and a single mutant neuron. *n* (13 for control and 7 for mutants) represents the number of total CA1 pyramidal neurons recorded. The thick blue lines in all beeswarm plots represent the respective median values. *P* values were computed with the Wilcoxon rank-sum test. Table 2 summarizes the means ± SE, and *P* values for measurements reported in this figure.

minimum of its temporal derivative dV/dt) were comparable between the CA1 pyramidal neurons from control and *Lhx2*$^{lox/lox}$ mice (Fig. 5, *D* and *E* and Table 2).

Together, despite changes in the biophysical properties of hippocampal astrocytes from the *Lhx2*$^{lox/lox}$ mice (Figs. 1, 2, and 3 and Table 1), the sub- and suprathreshold intrinsic properties of CA1 pyramidal neurons were not significantly different from controls (Figs. 4 and 5 and Table 2).

DISCUSSION

Astrocytes play a vital role in regulating neural circuit homeostasis, yet the transcriptional mechanisms governing their electrophysiological properties remain underexplored. In this study, we identify the LIM-homeodomain transcription factor LHX2 as a key regulator of the intrinsic electrical properties of astrocytes in the hippocampus. Our data demonstrate that deletion of *Lhx2* from postnatal progenitors alters their membrane biophysics in adulthood (Figs. 2 and 3).

Using whole cell current-clamp recordings, we showed that *Lhx2*-mutant astrocytes exhibit a hyperpolarized resting membrane potential and a pronounced increase in input resistance compared with controls, indicating enhanced steady-state electrical gain. In addition, we found that the measured input capacitance was consistently lower in mutant astrocytes compared with controls, despite the membrane time constant remaining comparable to controls. Increased input resistance and reduced input capacitance in mutant astrocytes are consistent with different possibilities such as reduced gap-junctional coupling across the astrocytic syncytium or smaller membrane surface area of the astrocytes. Furthermore, our analysis revealed no significant differences in sag or temporal summation—two indirect measures of resonant conductances—between control and mutant astrocytes. These findings suggest that the increased input resistance in

Table 2. *Statistical analyses of biophysical measurements of CA1 pyramidal neurons from control and Lhx2$^{lox/lox}$ mice*

	Measurements	Control	Mutant	*P* Value
1	Resting membrane potential, V_{RMP} (mV)	−62.6 ± 0.7	−61.3 ± 1.5	0.38
2	Input resistance, R_{in} (MΩ)	79.6 ± 9.4	72.9 ± 16.3	0.58
3	Summation ratio of αEPSPs, S_{α}	0.98 ± 0.07	0.84 ± 0.14	0.63
4	Sag, %	37.3 ± 3.4	30.6 ± 2.4	0.34
5	Maximal impedance amplitude, $\|Z\|_{max}$ (MΩ)	134.2 ± 14.7	139.9 ± 29.1	0.94
6	Resonance frequency, f_R (Hz)	3.9 ± 0.7	3.9 ± 0.6	1
7	Resonance strength, Q	1.4 ± 0.1	1.3 ± 0.08	1
8	Total inductive phase (Φ_L)	0.62 ± 0.14	0.65 ± 0.2	1
9	Action potential threshold, V_{th} (mV)	−41.5 ± 2.5	−48.4 ± 2.5	0.12
10	Action potential peak, V_{peak} (mV)	46.6 ± 2.5	42.4 ± 2.6	0.22
11	Action potential amplitude, V_{AP} (mV)	109.5 ± 2.41	101.9 ± 3.2	**0.03**
12	Action potential halfwidth, T_{APHW} (ms)	1.22 ± 0.13	1.15 ± 0.07	0.65
13	Peak dV/dt, $dV/dt\|_{max}$ (V/s)	386.9 ± 33.4	408.6 ± 33.0	0.85
14	Minimum dV/dt, $dV/dt\|_{min}$ (V/s)	−85.5 ± 7.46	−82.5 ± 5.6	0.58
15	Latency to first spike, T_{1AP} (ms)	41.8 ± 18.4	5.5 ± 1.22	0.17
16	First interspike interval, T_{1ISI} (ms)	57.3 ± 32.3	17.8 ± 4.1	1
17	Firing frequency at 50 pA, f_{50} (Hz)	0.5 ± 0.5	1.2 ± 0.6	0.13
18	Firing frequency at 100 pA, f_{100} (Hz)	4.6 ± 1.7	3.5 ± 1.5	0.86
19	Firing frequency at 150 pA, f_{150} (Hz)	9.4 ± 2.9	5.5 ± 2.2	0.47
20	Firing frequency at 200 pA, f_{200} (Hz)	15.1 ± 3.6	7.5 ± 2.9	0.18
21	Firing frequency at 250 pA, f_{250} (Hz)	19.4 ± 4.2	12.9 ± 3.3	0.44
22	Firing frequency at 500 pA, f_{500} (Hz)	31.9 ± 5.1	19.4 ± 3.5	0.13
23	Firing frequency at 750 pA, f_{750} (Hz)	32.2 ± 5.6	23.4 ± 5.5	0.39
24	Firing frequency at 1000 pA, f_{1000} (Hz)	37.1 ± 6.2	23.8 ± 7.4	0.27
25	Firing frequency at 1250 pA, f_{1250} (Hz)	34.9 ± 6.8	23.5 ± 8.8	0.25

Provided are the means ± SE values for the control and mutant group measurements. The *P* values correspond to the Wilcoxon rank-sum test. All *P* values less than 0.05 are highlighted in boldface font.

Lhx2-mutant astrocytes is unlikely to be due to changes in canonical resonant channels.

To further probe the dynamics of astrocyte responsiveness, we examined their frequency-dependent gain using a chirp stimulus that spanned a physiologically relevant range (0–15 Hz). Unlike CA1 pyramidal neurons, which show robust frequency-dependent resonance in this band (8, 9, 28), astrocytes displayed minimal variation in impedance amplitude and lacked strong resonance features. Importantly, mutant astrocytes showed a reduction in total inductive phase (Φ_L), which may reflect altered subthreshold ionic kinetics or capacitive properties. Nevertheless, the resonance frequency (f_R), maximal impedance ($|Z|_{max}$), and resonance strength (Q) were similar between groups. These findings highlight that while *Lhx2* deletion alters the static biophysical properties of astrocytes, their dynamic filtering capabilities remain largely intact.

In contrast to the substantial electrophysiological remodeling observed in astrocytes upon loss of *Lhx2*, the intrinsic properties of CA1 pyramidal neurons appeared largely unaffected (Figs. 4 and 5). Neither subthreshold parameters (resting potential, input resistance, sag, and temporal summation) nor frequency-dependent gain properties showed significant changes in mutant neurons. Suprathreshold analysis also revealed no difference in firing rates across a range of input currents, with the exception of a modest reduction in the action potential amplitude (Fig. 5). This isolated change did not extend to other action potential waveform metrics, including spike threshold, width, latency, or interspike intervals, suggesting that overall neuronal excitability remains preserved.

Lhx2 and Functional Characteristics of Adult Hippocampal Astrocytes

Traditionally viewed as passive support cells, astrocytes are now widely recognized as active and dynamic regulators of synaptic transmission, gliotransmission, learning and cognitive processes, metabolic homeostasis, ion buffering, and blood-brain barrier integrity (7, 15, 32–37). Astrocytes are integral components of the tripartite synapse, where they regulate neuronal synapse formation, maturation, function, and elimination through various secreted and contact-mediated signals (38–41). Astrocytes also modulate blood vessel growth and branching (42, 43), regulate blood flow in a neuronal activity-dependent manner (44, 45), and modulate nutrient uptake via their processes that wrap around blood vessels (46). Together, astrocytes are known to play critical roles in establishing and modulating neuron-glia functional circuitry.

Despite the several important roles of astrocytes, the molecular mechanisms that govern their intrinsic electrical properties—and how these properties influence or are influenced by developmental transcription factors—remain poorly understood. Our findings position LHX2 as a modulator of their biophysical identity, extending the roles of LHX2 beyond early gliogenesis into the regulation of mature astrocytic function. By integrating developmental genetics with precise electrophysiological profiling, this study underscores the importance of transcriptional programs in establishing astrocyte identity at a functional level. The demonstration that *Lhx2* deletion alters astrocyte membrane properties without significantly altering intrinsic neuronal excitability highlights the robustness of hippocampal circuits. It also raises important questions about how astrocytic changes

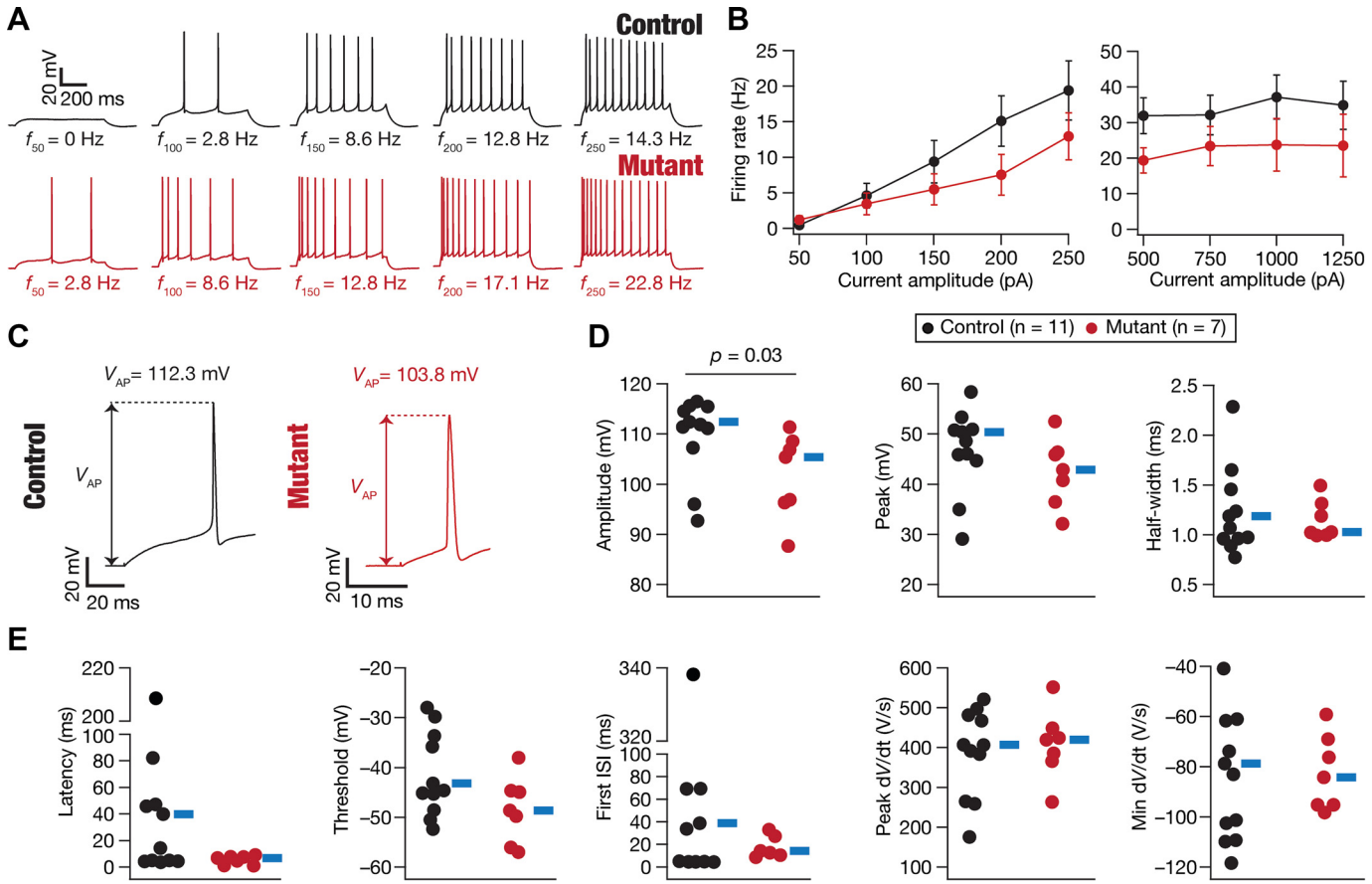

Figure 5. Suprathreshold electrophysiological properties of adult CA1 pyramidal neurons remained largely invariant to *Lhx2* mutation. *A*: voltage traces recorded in response to 50 pA to 250 pA, in steps of 50 pA, from control (*top*) and mutant (*bottom*) CA1 pyramidal neurons. The firing rate values associated with each trace are provided at the bottom of respective traces. *B*, *left*: plot showing firing rates of neurons from control and mutant groups (means ± SE), plotted against current injection amplitudes from 50 pA to 250 pA in steps of 50 pA. *Right*: firing rates of same set of neurons (means ± SE) for higher current injections ranging from 250 pA to 1,250 pA in steps of 250 pA. The firing rate values for none of the different current injection values showed significant differences between the control and the mutant groups. *C*: the first two action potentials in a spike train, recorded in response to a 250-pA current injection into the example neuron from control and mutant groups. Arrow marks the amplitude of first action potential V_{AP}, as measured from resting potential. *D*: beeswarm plots for action potential amplitude V_{AP}, peak ($P = 0.03$), half width ($P = 0.6$) calculated for the first action potential in response to 250 pA current injection for all control and mutant neurons. *E*: beeswarm plots for latency to first spike ($P = 0.17$), action potential threshold ($P = 0.12$), first interspike interval ($P = 1$), maximum value of temporal derivative *dV/dt* ($P = 0.86$), and the minimum value of temporal derivative *dV/dt* ($P = 0.58$) calculated from the first action potential in response to a 250 pA current injection of all control and mutant neurons. All illustrative example traces in this figure were taken from a single control and a single mutant neuron. *n* (11 for control and 7 for mutants) represents the number of total CA1 pyramidal neurons recorded. The thick blue lines in all beeswarm plots represent the respective median values. *P* values were computed with the Wilcoxon rank-sum test. Table 2 summarizes the means ± SE, and *P* values for measurements reported in this figure.

might affect other neuron-astrocyte interactions, such as synaptic modulation, neurotransmitter uptake, or plasticity. Furthermore, given the recognition of astrocyte dysfunction in neurological disorders (47–52), including epilepsy, Alzheimer's disease, and gliomas, understanding how transcription factors like *Lhx2* shape astrocyte behavior could inform new therapeutic strategies targeting glial cells rather than neurons.

Our study also provides a methodological framework for characterizing astrocyte excitability with dynamic, frequency-dependent inputs, a paradigm long established in neuronal research (8, 9, 22, 29, 53–64) but underutilized in glial physiology. Incorporating these approaches into astrocyte research may reveal previously unappreciated roles for astrocytes in neural computation and network oscillations. Specifically, impedance is a critical and effective measure of cellular excitability beyond what can be gleaned through pulse-current-based measures of excitability (8, 9, 22, 59–64). In the in vivo context that cells normally perform their functions, they encounter time-varying stimuli, with several brain structures, including the hippocampal structure, receiving inputs in well-defined oscillatory bands (25, 65). Therefore, there's a need to measure the excitability of cells with time-varying stimuli of different frequencies. Impedance measures offer not only quantification of frequency-dependent gain (computed as impedance amplitude) but also provide temporal relationship between response and stimulus through impedance phase (9, 60, 66). This temporal relationship is also frequency-dependent and provides crucial information on temporal integration of inputs coming through different frequencies (9, 66). Thus, impedance analyses offer critical physiological insights that go beyond what is observable with pulse-current-based inputs.

Our analyses did not provide evidence for membrane potential resonance in these astrocytes, potentially pointing to weak expression of resonating conductnces. However, the analysis technique could be useful for assessing channel expression profiles and their impact on cellular physiology in other astrocytes as well as in astrocytes in different pathological conditions. For instance, there could be glial channelopathies (15, 16, 67–70) involving upregulation of resonating or other conductances that are known to regulate resonance (22, 28, 58, 71–74) in astrocytes, which might yield resonance in the associated impedance profile. Thus, impedance offers a powerful tool to quantitatively analyze astrocytic physiology from the perspective of assessing frequency-dependent gain and temporal relationship in astrocytes across different brain regions, under different physiological and pathological conditions. Together, our work not only identifies a novel role for LHX2 in adult hippocampal astrocytes but also opens new avenues for exploring astrocyte contribution to circuit function and dysfunction from a systems neuroscience perspective.

Lhx2 and Functional Characteristics of Adult Hippocampal Pyramidal Neurons

In striking contrast to significant changes in astrocytic functional properties in $Lhx2^{lox/lox}$ mice, our analyses did not provide evidence for significant changes in intrinsic properties of hippocampal pyramidal neurons (Table 2) apart from significant changes in action potential amplitudes (Fig. 5 and Table 2). It is possible that signals from the mutant astrocytes were insufficient to perturb intrinsic neuronal excitability. However, alterations to the astrocytic transcriptome as a result of loss of *Lhx2* (2) could impact neuronal excitability and synaptic interactions.

The dissociation between astrocytic and neuronal responses raises intriguing possibilities. Future studies could examine whether loss of *Lhx2* in astrocytes modulates synaptic plasticity, circuit dynamics, or behavior, including in the context of aging, neurological disorders, or pathological conditions.

Limitations and future directions.

Although our study offers important insights into the role of LHX2 in regulating astrocyte biophysics and population dynamics, it has some caveats. First, our electrophysiological analysis was performed on acutely isolated brain slices under ex vivo conditions, which, while powerful for dissecting intrinsic membrane properties, do not fully capture the complexity of astrocyte behavior in the intact brain. Astrocytes in vivo are influenced by dynamic neuromodulatory, metabolic, and vascular cues that are absent in slice preparations, and these contextual factors could modulate their physiological state in ways not reflected in our data.

Second, although we used well-established current-clamp protocols, including chirp stimuli, to assess frequency-dependent gain and impedance properties, these approaches primarily characterize passive and subthreshold properties. Additional analyses incorporating voltage-clamp techniques, pharmacological manipulations, cell-attached recordings, or dynamic clamp simulations could provide more detailed insight into the specific ionic mechanisms affected by *Lhx2* deletion.

Third, while we identified clear changes in astrocyte membrane potential and input resistance, we did not directly measure downstream consequences on astrocyte-mediated functions such as neurotransmitter uptake, calcium signaling, or gliotransmitter release, metabolic and homeostatic functions, all of which could significantly affect circuit dynamics (15). Similarly, although the observed stability of neuronal intrinsic properties suggests resilience to altered astrocyte physiology, our study does not rule out more subtle effects on synaptic function or network-level behavior that could emerge under specific activity states or in response to experience-dependent plasticity. In addition, our focus in this study has been on astrocytes and pyramidal neurons. Future studies could explore potential effects on hippocampal interneurons and also examine interactions within the neuron-glia network (75–81), including through paired neuron-glia recordings.

Finally, as our interests were limited to long-term impact of *Lhx2* deletion, we measured electrophysiological properties at a single time point in adulthood. Although an ongoing role for LHX2 in mature astrocytes cannot be excluded, our findings open the door to further exploration across different time points. Similarly, the timeline of changes in neuronal physiological properties need to be carefully studied to assess if compensatory changes are at play in adulthood.

Future studies could focus on several important questions that remain. One critical next step is to elucidate the molecular mechanisms underlying the observed changes in astrocyte resting membrane potential and input resistance following *Lhx2* deletion. Another promising direction is to investigate how these changes in astrocyte physiology affect neuron-glia interactions at the synaptic level. Although intrinsic neuronal excitability appeared largely unaffected, astrocytes are known to influence neuronal activity through mechanisms such as potassium buffering, glutamate uptake, and gliotransmission. It will therefore be important to determine whether LHX2-mediated changes in astrocytes alter synaptic transmission, plasticity, or network oscillations.

As the hippocampus is central to learning and memory, future work should explore whether these cellular changes translate into measurable behavioral differences in hippocampus-dependent tasks. Finally, considering that astrocytes operate as a syncytium, it would be valuable to assess whether *Lhx2* loss affects properties such as gap junction coupling, calcium signaling, or metabolic support to neurons, which could have broader implications for circuit-level function.

Conclusion.

In this study, we identify *Lhx2* as a key regulator of biophysical properties of astrocytes in the hippocampus. Our finding that astrocyte membrane biophysics are modulated by a developmental transcription factor highlights the influence of early genetic perturbation on mature glial function. These results lay the groundwork for future investigations into how transcriptional control of astrocyte physiology contributes to circuit function, plasticity, and disease.

DATA AVAILABILITY

All data and associated analyses outcomes required for assessment of this study are available as part of the manuscript.

GRANTS

This work was funded by the DST INSPIRE Faculty Fellowship awarded to A.I. (Faculty Registration No: IFA18-LSBM210), the Department of Atomic Energy (DAE), Govt. of India (Project Identification No. RTI4003, DAE OM No. 1303/2/2019/R&D II/DAE/2079 to S.T.), and the Ministry of Education (to S.K. and R.N.).

DISCLOSURES

No conflicts of interest, financial or otherwise, are declared by the authors.

AUTHOR CONTRIBUTIONS

S.K., A.I., S.T., and R.N. conceived and designed research; S.K., A.I., performed experiments; S.K., A.I., analyzed data; S.K., A.I., S.T., and R.N. interpreted results of experiments; S.K., A.I., prepared figures; S.K., A.I., S.T., and R.N. drafted manuscript; S.K., A.I., S.T., and R.N. edited and revised manuscript; S.K., A.I., S.T., and R.N. approved final version of manuscript.

REFERENCES

1. **Chou SJ**, **Tole S.** Lhx2, an evolutionarily conserved, multifunctional regulator of forebrain development. *Brain Res* 1705: 1–14, 2019. doi:10.1016/j.brainres.2018.02.046.
2. **Iyer A**, **Fronteiro R**, **Bhatia P**, **Kumari S**, **Singh A**, **Zhou J**, **Bocchi R**, **Narayanan R**, **Tole S.** The transcription factor LHX2 suppresses astrocyte proliferation in the postnatal mammalian cerebral cortex. *Development* 152: dev204358, 2025. doi:10.1242/dev.204358.
3. **Mangale VS**, **Hirokawa KE**, **Satyaki PR**, **Gokulchandran N**, **Chikbire S**, **Subramanian L**, **Shetty AS**, **Martynoga B**, **Paul J**, **Mai MV**, **Li Y**, **Flanagan LA**, **Tole S**, **Monuki ES.** Lhx2 selector activity specifies cortical identity and suppresses hippocampal organizer fate. *Science* 319: 304–309, 2008. doi:10.1126/science.1151695.
4. **Porter FD**, **Drago J**, **Xu Y**, **Cheema SS**, **Wassif C**, **Huang SP**, **Lee E**, **Grinberg A**, **Massalas JS**, **Bodine D**, **Alt F**, **Westphal H.** Lhx2, a LIM homeobox gene, is required for eye, forebrain, and definitive erythrocyte development. *Development* 124: 2935–2944, 1997. doi:10.1242/dev.124.15.2935.
5. **Mishra P**, **Narayanan R.** Heterogeneities in intrinsic excitability and frequency-dependent response properties of granule cells across the blades of the rat dentate gyrus. *J Neurophysiol* 123: 755–772, 2020. doi:10.1152/jn.00443.2019.
6. **Mishra P**, **Narayanan R.** Conjunctive changes in multiple ion channels mediate activity-dependent intrinsic plasticity in hippocampal granule cells. *iScience* 25: 103922, 2022. doi:10.1016/j.isci.2022.103922.
7. **Ashhad S**, **Narayanan R.** Active dendrites regulate the impact of gliotransmission on rat hippocampal pyramidal neurons. *Proc Natl Acad Sci USA* 113: E3280–3289, 2016. doi:10.1073/pnas.1522180113.
8. **Narayanan R**, **Johnston D.** Long-term potentiation in rat hippocampal neurons is accompanied by spatially widespread changes in intrinsic oscillatory dynamics and excitability. *Neuron* 56: 1061–1075, 2007. doi:10.1016/j.neuron.2007.10.033.
9. **Narayanan R**, **Johnston D.** The h channel mediates location dependence and plasticity of intrinsic phase response in rat hippocampal neurons. *J Neurosci* 28: 5846–5860, 2008. doi:10.1523/JNEUROSCI.0835-08.2008.
10. **Rall W.** Time constants and electrotonic length of membrane cylinders and neurons. *Biophys J* 9: 1483–1508, 1969. doi:10.1016/S0006-3495(69)86467-2.
11. **Mittal D**, **Narayanan R.** Degeneracy in the robust expression of spectral selectivity, subthreshold oscillations, and intrinsic excitability of entorhinal stellate cells. *J Neurophysiol* 120: 576–600, 2018. doi:10.1152/jn.00136.2018.
12. **Miller FD**, **Gauthier AS.** Timing is everything: making neurons versus glia in the developing cortex. *Neuron* 54: 357–369, 2007. doi:10.1016/j.neuron.2007.04.019.
13. **Ganat YM**, **Silbereis J**, **Cave C**, **Ngu H**, **Anderson GM**, **Ohkubo Y**, **Ment LR**, **Vaccarino FM.** Early postnatal astroglial cells produce multilineage precursors and neural stem cells in vivo. *J Neurosci* 26: 8609–8621, 2006. doi:10.1523/JNEUROSCI.2532-06.2006.
14. **Madisen L**, **Zwingman TA**, **Sunkin SM**, **Oh SW**, **Zariwala HA**, **Gu H**, **Ng LL**, **Palmiter RD**, **Hawrylycz MJ**, **Jones AR**, **Lein ES**, **Zeng H. A.** robust and high-throughput Cre reporting and characterization system for the whole mouse brain. *Nat Neurosci* 13: 133–140, 2010. doi:10.1038/nn.2467.
15. **Verkhratsky A**, **Nedergaard M.** Physiology of astroglia. *Physiol Rev* 98: 239–389, 2018. doi:10.1152/physrev.00042.2016.
16. **Verkhratsky A**, **Steinhauser C.** Ion channels in glial cells. *Brain Res Brain Res Rev* 32: 380–412, 2000. doi:10.1016/s0165-0173(99)00093-4.
17. **Magee JC.** Dendritic hyperpolarization-activated currents modify the integrative properties of hippocampal CA1 pyramidal neurons. *J Neurosci* 18: 7613–7624, 1998. doi:10.1523/JNEUROSCI.18-19-07613.1998.
18. **Hönigsperger C**, **Marosi M**, **Murphy R**, **Storm JF.** Dorsoventral differences in Kv7/M-current and its impact on resonance, temporal summation and excitability in rat hippocampal pyramidal cells. *J Physiol* 593: 1551–1580, 2015. doi:10.1113/jphysiol.2014.280826.
19. **Hu H**, **Vervaeke K**, **Graham LJ**, **Storm JF.** Complementary theta resonance filtering by two spatially segregated mechanisms in CA1 hippocampal pyramidal neurons. *J Neurosci* 29: 14472–14483, 2009. doi:10.1523/JNEUROSCI.0187-09.2009.
20. **Hu H**, **Vervaeke K**, **Storm JF.** M-channels (Kv7/KCNQ channels) that regulate synaptic integration, excitability, and spike pattern of CA1 pyramidal cells are located in the perisomatic region. *J Neurosci* 27: 1853–1867, 2007. doi:10.1523/JNEUROSCI.4463-06.2007.
21. **Mateos-Aparicio P**, **Murphy R**, **Storm JF.** Complementary functions of SK and Kv7/M potassium channels in excitability control and synaptic integration in rat hippocampal dentate granule cells. *J Physiol* 592: 669–693, 2014. doi:10.1113/jphysiol.2013.267872.
22. **Mishra P**, **Narayanan R.** The enigmatic HCN channels: a cellular neurophysiology perspective. *Proteins* 93: 72–92, 2025. doi:10.1002/prot.26643.
23. **Buzsaki G.** Theta oscillations in the hippocampus. *Neuron* 33: 325–340, 2002. doi:10.1016/S0896-6273(02)00586-X.
24. **Colgin LL.** Mechanisms and functions of theta rhythms. *Annu Rev Neurosci* 36: 295–312, 2013. doi:10.1146/annurev-neuro-062012-170330.
25. **Colgin LL.** Rhythms of the hippocampal network. *Nat Rev Neurosci* 17: 239–249, 2016. doi:10.1038/nrn.2016.21.
26. **Wang DS**, **Ju L**, **Pinguelo AG**, **Kaneshwaran K**, **Haffey SC**, **Lecker I**, **Gohil H**, **Wheeler MB**, **Kaustov L**, **Ariza A**, **Yu M**, **Volchuk A**, **Steinberg BE**, **Goldenberg NM**, **Orser BA.** Crosstalk between GABA(A) receptors in astrocytes and neurons triggered by general anesthetic drugs. *Transl Res* 267: 39–53, 2024. doi:10.1016/j.trsl.2023.11.007.
27. **Zhou M**, **Kimelberg HK.** Freshly isolated hippocampal CA1 astrocytes comprise two populations differing in glutamate transporter and AMPA receptor expression. *J Neurosci* 21: 7901–7908, 2001. doi:10.1523/JNEUROSCI.21-20-07901.2001.
28. **Hu H**, **Vervaeke K**, **Storm JF.** Two forms of electrical resonance at theta frequencies, generated by M-current, h-current and persistent Na+ current in rat hippocampal pyramidal cells. *J Physiol* 545: 783–805, 2002. doi:10.1113/jphysiol.2002.029249.
29. **Gimbarzevsky B**, **Miura RM**, **Puil E.** Impedance profiles of peripheral and central neurons. *Can J Physiol Pharmacol* 62: 460–462, 1984. doi:10.1139/y84-074.
30. **Brager DH**, **Akhavan AR**, **Johnston D.** Impaired dendritic expression and plasticity of h-channels in the fmr1(-/y) mouse model of fragile X syndrome. *Cell Rep* 1: 225–233, 2012. doi:10.1016/j.celrep.2012.02.002.
31. **Brandalise F**, **Kalmbach BE**, **Mehta P**, **Thornton O**, **Johnston D**, **Zemelman BV**, **Brager DH.** Fragile X mental retardation protein bidirectionally controls dendritic Ih in a cell type-specific manner between mouse hippocampus and prefrontal cortex. *J Neurosci* 40: 5327–5340, 2020. doi:10.1523/JNEUROSCI.1670-19.2020.
32. **Ashhad S**, **Narayanan R.** Stores, channels, glue, and trees: active glial and active dendritic physiology. *Mol Neurobiol* 56: 2278–2299, 2019. doi:10.1007/s12035-018-1223-5.
33. **Kol A**, **Goshen I.** The memory orchestra: the role of astrocytes and oligodendrocytes in parallel to neurons. *Curr Opin Neurobiol* 67: 131–137, 2021. doi:10.1016/j.conb.2020.10.022.

34. **Bazargani N**, **Attwell D.** Astrocyte calcium signaling: the third wave. *Nat Neurosci* 19: 182–189, 2016. doi:10.1038/nn.4201.
35. **Khakh BS**, **Sofroniew MV.** Diversity of astrocyte functions and phenotypes in neural circuits. *Nat Neurosci* 18: 942–952, 2015. doi:10.1038/nn.4043.
36. **Santello M**, **Toni N**, **Volterra A.** Astrocyte function from information processing to cognition and cognitive impairment. *Nat Neurosci* 22: 154–166, 2019. doi:10.1038/s41593-018-0325-8.
37. **Araque A**, **Carmignoto G**, **Haydon PG**, **Oliet SH**, **Robitaille R**, **Volterra A.** Gliotransmitters travel in time and space. *Neuron* 81: 728–739, 2014. doi:10.1016/j.neuron.2014.02.007.
38. **Farhy-Tselnicker I**, **Boisvert MM**, **Liu H**, **Dowling C**, **Erikson GA**, **Blanco-Suarez E**, **Farhy C**, **Shokhirev MN**, **Ecker JR**, **Allen NJ.** Activity-dependent modulation of synapse-regulating genes in astrocytes. *Elife* 10: e70514, 2021. doi:10.7554/eLife.70514.
39. **Allen NJ**, **Eroglu C.** Cell biology of astrocyte-synapse interactions. *Neuron* 96: 697–708, 2017. doi:10.1016/j.neuron.2017.09.056.
40. **Stogsdill JA**, **Ramirez J**, **Liu D**, **Kim YH**, **Baldwin KT**, **Enustun E**, **Ejikeme T**, **Ji RR**, **Eroglu C.** Astrocytic neuroligins control astrocyte morphogenesis and synaptogenesis. *Nature* 551: 192–197, 2017. doi:10.1038/nature24638.
41. **Clarke LE**, **Barres BA.** Emerging roles of astrocytes in neural circuit development. *Nat Rev Neurosci* 14: 311–321, 2013 [Erratum in *Nat Rev Neurosci* 14: 451, 2013]. doi:10.1038/nrn3484.
42. **Ma S**, **Kwon HJ**, **Huang Z.** A functional requirement for astroglia in promoting blood vessel development in the early postnatal brain. *PLoS One* 7: e48001, 2012. doi:10.1371/journal.pone.0048001.
43. **Tabata H**, **Sasaki M**, **Agetsuma M**, **Sano H**, **Hirota Y**, **Miyajima M**, **Hayashi K**, **Honda T**, **Nishikawa M**, **Inaguma Y**, **Ito H**, **Takebayashi H**, **Ema M**, **Ikenaka K**, **Nabekura J**, **Nagata KI**, **Nakajima K.** Erratic and blood vessel-guided migration of astrocyte progenitors in the cerebral cortex. *Nat Commun* 13: 6571, 2022. doi:10.1038/s41467-022-34184-x.
44. **MacVicar BA**, **Newman EA.** Astrocyte regulation of blood flow in the brain. *Cold Spring Harb Perspect Biol* 7: a020388, 2015. doi:10.1101/cshperspect.a020388.
45. **Otsu Y**, **Couchman K**, **Lyons DG**, **Collot M**, **Agarwal A**, **Mallet JM**, **Pfrieger FW**, **Bergles DE**, **Charpak S.** Calcium dynamics in astrocyte processes during neurovascular coupling. *Nat Neurosci* 18: 210–218, 2015. doi:10.1038/nn.3906.
46. **Barres BA.** The mystery and magic of glia: a perspective on their roles in health and disease. *Neuron* 60: 430–440, 2008. doi:10.1016/j.neuron.2008.10.013.
47. **Maragakis NJ**, **Rothstein JD.** Mechanisms of Disease: astrocytes in neurodegenerative disease. *Nat Clin Pract Neurol* 2: 679–689, 2006. doi:10.1038/ncpneuro0355.
48. **Parpura V**, **Heneka MT**, **Montana V**, **Oliet SH**, **Schousboe A**, **Haydon PG**, **Stout RF Jr**, **Spray DC**, **Reichenbach A**, **Pannicke T**, **Pekny M**, **Pekna M**, **Zorec R**, **Verkhratsky A.** Glial cells in (patho)physiology. *J Neurochem* 121: 4–27, 2012. doi:10.1111/j.1471-4159.2012.07664.x.
49. **Patel DC**, **Tewari BP**, **Chaunsali L**, **Sontheimer H.** Neuron-glia interactions in the pathophysiology of epilepsy. *Nat Rev Neurosci* 20: 282–297, 2019. doi:10.1038/s41583-019-0126-4.
50. **Mega A**, **Hartmark Nilsen M**, **Leiss LW**, **Tobin NP**, **Miletic H**, **Sleire L**, **Strell C**, **Nelander S**, **Krona C**, **Hagerstrand D**, **Enger PO**, **Nister M**, **Ostman A.** Astrocytes enhance glioblastoma growth. *Glia* 68: 316–327, 2020. doi:10.1002/glia.23718.
51. **Habib N**, **McCabe C**, **Medina S**, **Varshavsky M**, **Kitsberg D**, **Dvir-Szternfeld R**, **Green G**, **Dionne D**, **Nguyen L**, **Marshall JL**, **Chen F**, **Zhang F**, **Kaplan T**, **Regev A**, **Schwartz M.** Disease-associated astrocytes in Alzheimer's disease and aging. *Nat Neurosci* 23: 701–706, 2020. doi:10.1038/s41593-020-0624-8.
52. **Vezzani A**, **Ravizza T**, **Bedner P**, **Aronica E**, **Steinhauser C**, **Boison D.** Astrocytes in the initiation and progression of epilepsy. *Nat Rev Neurol* 18: 707–722, 2022. doi:10.1038/s41582-022-00727-5.
53. **Puil E**, **Gimbarzevsky B**, **Miura RM.** Quantification of membrane properties of trigeminal root ganglion neurons in guinea pigs. *J Neurophysiol* 55: 995–1016, 1986. doi:10.1152/jn.1986.55.5.995.
54. **Puil E**, **Gimbarzevsky B**, **Spigelman I.** Primary involvement of K+ conductance in membrane resonance of trigeminal root ganglion neurons. *J Neurophysiol* 59: 77–89, 1988. doi:10.1152/jn.1988.59.1.77.
55. **Hutcheon B**, **Miura RM**, **Puil E.** Models of subthreshold membrane resonance in neocortical neurons. *J Neurophysiol* 76: 698–714, 1996. doi:10.1152/jn.1996.76.2.698.
56. **Hutcheon B**, **Miura RM**, **Puil E.** Subthreshold membrane resonance in neocortical neurons. *J Neurophysiol* 76: 683–697, 1996. doi:10.1152/jn.1996.76.2.683.
57. **Hutcheon B**, **Miura RM**, **Yarom Y**, **Puil E.** Low-threshold calcium current and resonance in thalamic neurons: a model of frequency preference. *J Neurophysiol* 71: 583–594, 1994. doi:10.1152/jn.1994.71.2.583.
58. **Hutcheon B**, **Yarom Y.** Resonance, oscillation and the intrinsic frequency preferences of neurons. *Trends Neurosci* 23: 216–222, 2000. doi:10.1016/s0166-2236(00)01547-2.
59. **Cole KS.** Electric impedance of suspensions of Arbacia eggs. *J Gen Physiol* 12: 37–54, 1928. doi:10.1085/jgp.12.1.37.
60. **Cole KS.** Electric phase angle of cell membranes. *J Gen Physiol* 15: 641–649, 1932. doi:10.1085/jgp.15.6.641.
61. **Cole KS.** Electric impedance of Hipponoe eggs. *J Gen Physiol* 18: 877–887, 1935. doi:10.1085/jgp.18.6.877.
62. **Cole KS.** Rectification and inductance in the squid giant axon. *J Gen Physiol* 25: 29–51, 1941. doi:10.1085/jgp.25.1.29.
63. **Cole KS**, **Baker RF.** Transverse impedance of the squid giant axon during current flow. *J Gen Physiol* 24: 535–549, 1941. doi:10.1085/jgp.24.4.535.
64. **Mauro A**, **Conti F**, **Dodge F**, **Schor R.** Subthreshold behavior and phenomenological impedance of the squid giant axon. *J Gen Physiol* 55: 497–523, 1970. doi:10.1085/jgp.55.4.497.
65. **Wang XJ.** Neurophysiological and computational principles of cortical rhythms in cognition. *Physiol Rev* 90: 1195–1268, 2010. doi:10.1152/physrev.00035.2008.
66. **Vaidya SP**, **Johnston D.** Temporal synchrony and gamma-to-theta power conversion in the dendrites of CA1 pyramidal neurons. *Nat Neurosci* 16: 1812–1820, 2013. doi:10.1038/nn.3562.
67. **Hanslik KL**, **Marino KM**, **Ulland TK.** Modulation of glial function in health, aging, and neurodegenerative disease. *Front Cell Neurosci* 15: 718324, 2021. doi:10.3389/fncel.2021.718324.
68. **Lia A**, **Di Spiezio A**, **Vitalini L**, **Tore M**, **Puja G**, **Losi G.** Ion channels and ionotropic receptors in astrocytes: physiological functions and alterations in Alzheimer's disease and glioblastoma. *Life (Basel)* 13: 2038, 2023. doi:10.3390/life13102038.
69. **Wang S**, **Wang B**, **Shang D**, **Zhang K**, **Yan X**, **Zhang X.** Ion channel dysfunction in astrocytes in neurodegenerative diseases. *Front Physiol* 13: 814285, 2022. doi:10.3389/fphys.2022.814285.
70. **Leandrou E**, **Chalatsa I**, **Anagnostou D**, **Machalia C**, **Semitekolou M**, **Filippa V**, **Makridakis M**, **Vlahou A**, **Anastasiadou E**, **Vekrellis K**, **Emmanouilidou E.** alpha-Synuclein oligomers potentiate neuroinflammatory NF-kappaB activity and induce Ca(v)3.2 calcium signaling in astrocytes. *Transl Neurodegener* 13: 11, 2024. doi:10.1186/s40035-024-00401-4.
71. **Rathour RK**, **Malik R**, **Narayanan R.** Transient potassium channels augment degeneracy in hippocampal active dendritic spectral tuning. *Sci Rep* 6: 24678, 2016. doi:10.1038/srep24678.
72. **Rathour RK**, **Narayanan R.** Inactivating ion channels augment robustness of subthreshold intrinsic response dynamics to parametric variability in hippocampal model neurons. *J Physiol* 590: 5629–5652, 2012. doi:10.1113/jphysiol.2012.239418.
73. **Rathour RK**, **Narayanan R.** Homeostasis of functional maps in active dendrites emerges in the absence of individual channelostasis. *Proc Natl Acad Sci USA* 111: E1787–1796, 2014. doi:10.1073/pnas.1316599111.
74. **Rathour RK**, **Narayanan R.** Degeneracy in hippocampal physiology and plasticity. *Hippocampus* 29: 980–1022, 2019. doi:10.1002/hipo.23139.
75. **Buzsaki G.** Hippocampal GABAergic interneurons: a physiological perspective. *Neurochem Res* 26: 899–905, 2001. doi:10.1023/a:1012324231897.
76. **Bezaire MJ**, **Soltesz I.** Quantitative assessment of CA1 local circuits: knowledge base for interneuron-pyramidal cell connectivity. *Hippocampus* 23: 751–785, 2013. doi:10.1002/hipo.22141.
77. **Deemyad T**, **Luthi J**, **Spruston N.** Astrocytes integrate and drive action potential firing in inhibitory subnetworks. *Nat Commun* 9: 4336, 2018. doi:10.1038/s41467-018-06338-3.

78. **Pabst M**, **Braganza O**, **Dannenberg H**, **Hu W**, **Pothmann L**, **Rosen J**, **Mody I**, **van Loo K**, **Deisseroth K**, **Becker AJ**, **Schoch S**, **Beck H.** Astrocyte intermediaries of septal cholinergic modulation in the hippocampus. *Neuron* 90: 853–865, 2016. doi:10.1016/j.neuron.2016.04.003.
79. **Matos M**, **Bosson A**, **Riebe I**, **Reynell C**, **Vallee J**, **Laplante I**, **Panatier A**, **Robitaille R**, **Lacaille JC.** Astrocytes detect and upregulate transmission at inhibitory synapses of somatostatin interneurons onto pyramidal cells. *Nat Commun* 9: 4254, 2018. doi:10.1038/s41467-018-06731-y.
80. **Ngoc KH**, **Jeon Y**, **Ko J**, **Um JW.** Multifarious astrocyte-neuron dialog in shaping neural circuit architecture. *Trends Cell Biol* 35: 74–87, 2025. doi:10.1016/j.tcb.2024.05.002.
81. **Kwon W**, **Williamson MR**, **Deneen B.** A functional perspective on astrocyte heterogeneity. *Trends Neurosci* 48: 691–705, 2025. doi:10.1016/j.tins.2025.06.009.